11-2016

High Pressure Line Shapes of the Rb D_1 and D_2 lines for ^{4}He and ^{3}He Collisions

Wooddy S. Miller

Christopher A. Rice
Air Force Institute of Technology

Gordon D. Hager

Matthew D. Rotondaro

Hamid Berriche

See next page for additional authors

Recommended Citation

Miller, W. S., Rice, C. A., Hager, G. D., Rotondaro, M. D., Berriche, H., & Perram, G. P. (2016). High pressure line shapes of the Rb {D1} and {D2} lines for 4He and 3He collisions. Journal of Quantitative Spectroscopy and Radiative Transfer, 184, 118–134. https://doi.org/10.1016/j.jqsrt.2016.06.027

Version of Record: https://www.sciencedirect.com/science/article/pii/S0022407316301170
Manuscript_801a94f499d9e4d05b2b3570d0c21dc8

High Pressure Line shapes of the Rb D_1 and D_2 lines for ^{4}He and ^{3}He collisions

Wooddy S. Miller[1], Christopher A. Rice[2], Gordon D. Hager[3], Mathew D. Rotondaro[4], Hamid Berriche[5,a,b], Glen P. Perram[6]

Department of Engineering Physics
Air Force Institute of Technology
Wright-Patterson AFB, OH, United States, 45433-7765

[a] *Laboratory of Interfaces and Advanced Materials*
Faculty of Science, University of Monastir
Avenue de l'Environnement, 5019 Monastir, Tunisia
[b] *Mathematics and Natural Sciences Department*
School of Arts and Sciences, American University of Ras Al Khaimah
Ras Al Khaimah, P. O. Box,10021, UAE

Abstract

Line shapes for the Rb D_1 ($5\ ^2S_{1/2} \leftrightarrow 5\ ^2P_{1/2}$) and D_2 ($5\ ^2S_{1/2} \leftrightarrow 5\ ^2P_{3/2}$) transitions with ^{4}He and ^{3}He collisions at pressures of 500 - 15,000 Torr and temperatures of 333 - 533 K have been experimentally observed and compared to predictions from the Anderson-Talman theory. The ground $X^2\Sigma^+_{1/2}$ and excited $A^2\Pi_{1/2}$, $A^2\Pi_{3/2}$, and $B^2\Sigma^+_{1/2}$ potential energy surfaces required for the line shape predictions have been calculated using a one-electron pseudo-potential technique. The observed collision induced shift rates for ^{4}He are dramatically higher for the D_1 line, 4.60 ± 0.12 MHz/Torr than the D_2 line, 0.20 ± 0.14 MHz/Torr. The asymmetry is somewhat larger for the D_1 line and has the same sign as the shifting rate. The ^{3}He broadening rate for the D_2 line is 4% larger than the ^{4}He rate, and 14% higher for the D_1 line, reflecting the higher relative speed. The calculated broadening rates are systematically larger than the observed rates by 1.1 - 3.2 MHz/Torr and agree within 14%. The primary focus of the current work is to characterize the high pressure line shapes, focusing on the non-Lorentzian features far from line center. In the far wing, the cross-section decreases by more than 4 orders of magnitude, with a broad, secondary maximum in the D_2 line near 735 nm. The potentials do not require empirical modification to provide excellent quantitative agreement with the observations. The dipole moment variation and absorption Boltzmann factor is critical to obtaining strong agreement in the wings.

Keywords:
line shape, rubidium, asymmetric broadening, potentials

1. Introduction

The diode-pumped alkali laser (DPAL) was proposed in 2001 as an alternative to high-power, diode-pumped, solid-state lasers (28; 30). The radiation from the un-phased diode laser bars or stacks are absorbed on the D_2 $^2S_{1/2} \rightleftarrows {}^2P_{3/2}$ transition and collisional energy transfer to the spin-orbit split $^2P_{1/2}$ state yields lasing on the D_1 $^2P_{1/2} \rightleftarrows {}^2S_{1/2}$ transition in potassium, rubidium, or cesium vapor.

A rubidium laser pumped by a 1.28 kW diode stack with a 0.35-nm bandwidth has achieved 145-W average power (52). More recently, 1 kW Cs laser with closed loop transverse flow was demonstrated with 48% optical-to-optical efficiency (11). The fine structure splitting in Cs is large, and hydrocarbon collision partners are generally required to prevent bottlenecking. The presence of hydrocarbons can lead to soot and alkali hydride formation (29). In contrast, helium is sufficient to induce fine structure mixing in Rb with the rates required to support high power development (36). Helium pressures of 10-20 atmospheres are required to avoid bottlenecking on the fine structure mixing and to broaden the absorption line shapes sufficiently to accept modestly narrowed diode bar radiation. Characterizing the high pressure Rb-He line shapes is critical to: (1) design the pump diode spectral band, (2) design the optical resonator, (3) assess the effects of atmospheric transmission on high power propagation, and (4) evaluate the rates of ionization via far wing absorption. In this chapter we observe and compare with theory the high-pressure line shapes for the Rb D_1 and D_2 lines induced by collisions with ^{4}He and ^{3}He.

The Rb-He gas line shapes near resonance (in the core) have been investigated experimentally in considerable detail (45; 44; 51; 42; 34; 40; 23; 47; 6; 25; 49; 19; 27). The broadening and shifting rates for the Rb D_1 line induced by collisions with ^{4}He using modern methods agree to within better than 4% (45; 44; 51; 42; 34). The agreement for the D_2 line is poorer, with a 9% variance for the broadening rate and 20% for the shift rate. The shift rate for the D_2 line is small due to the combined

[1] Wooddy.S.Miller.mil@mail.mil
[2] Christopher.Rice@afit.edu; Secondary affiliation: Oak Ridge Institute for Science and Education
[3] drydoc12@comcast.net
[4] rotondam@gmail.com
[5] hamidberriche@yahoo.fr
[6] Corresponding author, glen.perram@afit.edu, 937-255-3636 x 4504

effects of two electronic surfaces. The temperature range where these rates have been determined is modest, 314-394 K, and span several different studies. Older measurements during the period 1940-1980 exhibit a 30% variance in broadening rates and disagree on the sign of the shift (40; 23; 47; 6; 25; 49; 19). The corresponding rates for collisions with ^{3}He were all performed at high pressures, >1 atm, and vary by about 20% (44; 27; 32).

Several computational approaches have also been applied to compute the broadening and shift rates (26; 46; 9; 33; 8). However, the results are sensitive to the long range portion of the interaction potentials. Indeed, the two ab inito potentials (35; 10) used in our recent study of Cs line shapes (20) both require empirical modification to adequately describe the observed spectra. Furthermore, different line shape theories applied to the same interaction potentials do not agree on the sign of the shift for the Rb-He interaction (9).

In the current work we focus on the high pressure, non-Lorentzian behavior of the Rb-He D_1 and D_2 line shapes. For pressures exceeding 1,000 Torr, a significant asymmetry has been observed in the core of the line, (44; 42; 34) as predicted by several theoretical calculations (12; 13; 17; 24). However, the magnitude of the asymmetry is not well predicted and further refinement of the interaction potential appears necessary (26). A blue satellite is observed in the far wing of the Rb D_2 line and is most pronounced for the heavier rare gases (12; 13; 17; 24; 2). A comparison of the theoretical predictions for the far wing spectra of Rb-He over a broad range of temperatures has recently been published (12). In the recent work, potential surfaces were generated using SA-CASSCF-MRCI calculations. In this paper we report observations of the absorption spectrum in far wings of the Rb D_2 and D_1 lines perturbed by ^{4}He and ^{3}He at pressures as high as 15,000 Torr. We then employ the Anderson-Talman theory, (3; 4) including the effects of dipole moment variation, (1) to predict the line shapes. The sensitivity of dipole moment variation on the wing line shapes is also evaluated. Our longer-term goal is to unify the Rb-He DPAL kinetics with potential surfaces that are sufficient to predict the temperature dependence of the fine structure mixing rates and collisional line shape parameters.

2. Experiment

Absorption spectra for rubidium vapor in the spectral range 600-875 nm were observed using a grating monochromator, as shown in Figure 1. The broadband visible emission from an Ealing 100 Watt tungsten lamp, with Oriel 68831 300 W lamp power supply, was collimated with an f=2.5 cm lens to pass through a Rb sample maintained in a gas recirculation cell. The transmitted light was focused with another f=2.5 cm, 5 cm diameter lens onto the entrance slit of a McPherson model 209 f=1.33 m (f/#=9.4) monochromator. With a 500 nm blaze, 1200 gr/mm grating and slits widths of 20.8 μm for the entrance and 34.7 μm for the exit, the instrumental line shape exhibited a full width at half maximum spectral resolution of 0.05 nm (24.7 GHz). An Ultraviolet Products krypton pen lamp was positioned at 17 mm in front of the monochromator entrance slit to provide dynamic wavelength calibration. Wavelength calibration was stable to within 0.035 nm from over 6 months of data acquisition. Wavelength calibrations were performed dynamically, with the lamp and absorption spectra acquired simultaneously. During a single run, the accuracy of the calibration was limited to about 10% of the instrumental line shape. At 15,000 Torr, this corresponds to an uncertainty is shift and broadening rates of about 0.17 MHz/Torr.

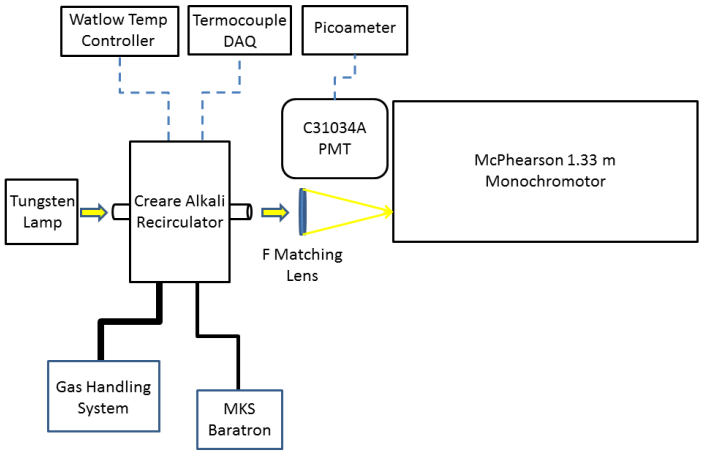

Figure 1: Experimental setup for the High-Pressure Lineshape Study

An uncooled Burle C31034A photomultiplier tube biased at 1,275 V exhibited a dark signal bias of 4-6 nA with noise fluctuation of 0.04 nA, as monitored on a Keithley model 386 picoammeter with 0.175 integration time. Monochromator scan rates of 0.32 nm/min required approximately 11 hours to obtain a full spectrum across the range 670-880 nm. The spectrum is sampled 11 times for each digital step in wavelength of 0.01 nm. The un-attenuated lamp signal was typically 110-120 nA with noise of 0.25-0.35 nA. The minimum detectable absorbance:

$$A = -ln\left[I_t(\lambda)/I_0(\lambda)\right] \quad (1)$$

where

$I_t(\lambda)$ = transmitted intensity with Rb vapor in the path

$I_o(\lambda)$ = transmitted intensity without Rb in the path

was limited by the detector noise at A= 0.005. The maximum detectable absorbance was limited by baseline drift and noise at A= 2.1. Absorbance was stable to within 2% over a 13-hour period for a cold cell. Cell window transmission degraded by about 60% over a 6-month period. This long-term window cleanliness was likely a result of: (1) the absence of hydrocarbons in the cell, (2) low irradiance from the white light source (no laser irradiation), (3) maintaining elevated window temperatures, and most importantly (4) minimizing outgassing, and alkali handling in a glove box environment.

A spectral baseline, $I_o(\lambda)$, was obtained by recording the transmitted intensity with the circulator operated at 296 K (Rb density, $n < 10^{10} atom/cm^3$) and evacuated conditions to minimize the spectral absorption. A 9^{th} order polynomial fit for the

average of several observed baselines before and after allows interpolation across the weak and narrow D_1 and D_2 line positions. This baseline had no theoretical basis and was chosen because it provided the best fit to the cold scan data. The stability of the observed baselines was affected primarily by changes in the circulator window transmission. The transmitted signal at 735 nm with the circulator operating at 513 K varied from 38.5-41.0 nA, or by 6.5% during a 13 hour observation.

A schematic of the gas circulator and gas handling system is provided in Figure 2. The gas bearing turbo machinery circulator provides mass flow rates of up to 1 g/s to enable future laser demonstrations. In the current experiments, stagnant, non-flowing circulator conditions were employed. The Monel 400 walls and stainless steel 316 valves were not degraded throughout the testing period. The optical path length with Rb vapor is 8.125 cm and accessed through 4 fused silica windows. The space between the double windows on each end of the cell were evacuated and designed to minimize thermal gradient induced turbulence. Custom made Monel 400 gaskets, made softer by annealing, were used in place of traditional OFHC Copper gaskets on all CF seals. Temperatures of 333-533 K were monitored by type K thermocouples and controlled in four zones with a Watlow controller, to yield rubidium densities of n = 2.5 x 10^{11} - 6.3 x 10^{15} atoms/cm^3. The windows were kept at 5-10 K hotter than the test cell to minimize plating. Rubidium density is stable to within 2% over a 13 hour period. However, there is a periodic variation of temperature, due to the control system response time of 3.5 min, of ΔT = 3 K. This produces a variation in absorbance of up to ΔA = .02 at the highest temperatures, and is corrected as discussed below.

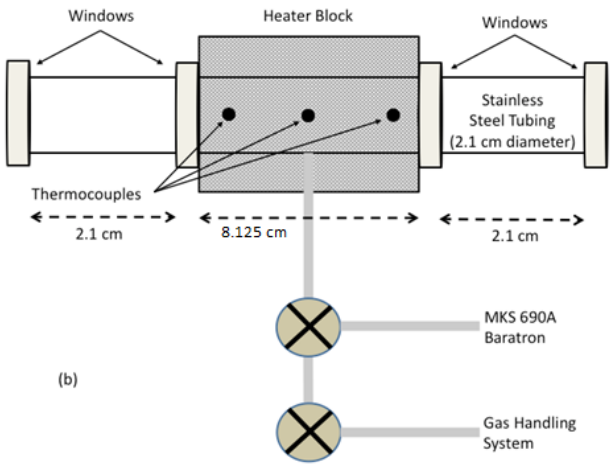

Figure 2: Diagram of the high-pressure Rb absorption cell

Approximately 1 g of Alfa Aesar 99.75% purity, natural isotopic abundance rubidium was loaded into the circulator in a nitrogen purged dry box. This single charge of rubidium was not depleted or reacted during the 9 months of operation. Linde 99.9999% ^{4}He and Spectra Gases, 99.9% ^{3}He was introduced through a SAES heated getter and 0.003 μm filter to remove atmospheric gases, CO, and H_2 to <1 ppb. A Varian EX9698996 turbo pump was used to evacuate the circulator. Pressure was measured with a 15,000 Torr MKS model 609A manometer and 670 signal conditioner. Line shapes for gas pressures of 500 - 15,000 Torr were observed. Pressure measurements are performed and reported at the elevated cell temperatures. The pressure transducer is protected behind a stainless steel valve during the longer spectral scans.

3. Observed Spectra

The transmitted intensity as a function of monochromator wavelength for several rubidium densities and ^{4}He pressure of 10,000 Torr is provided in Figure 3. The various spectral features are assigned to the strongly absorbed Rb D_1 and D_2 lines, the weaker Cs D_2 line at 852.1 nm due to sample impurity, the Kr lamp calibration lines, and for the higher Rb densities, the vibrational bands of the Rb_2 $X^1\Sigma_{g^+} - B^1\Pi_u$ electronic transition. The broad blue satellite of the Rb D_2 line can also been seen in the higher Rb density scans near λ = 735 nm. The absorbance in the blue satellite is 0.03% of the line center absorbance at 10,000 Torr. The core of the Rb D_2 and D_1 lines become highly opaque for T > 400 K. The relative height of the Cs D_2 line suggests ~0.047% Cs in the sample. The potassium lines near 770 nm and 766 nm are very weak in the current spectra. At T = 333 K, the ratio of Rb dimer to atom concentrations is 7×10^{-5} and grows dramatically to 4×10^{-3} at T = 533 K (39). Fortunately the Rb_2 absorbance is spectrally isolated from the atomic lines.

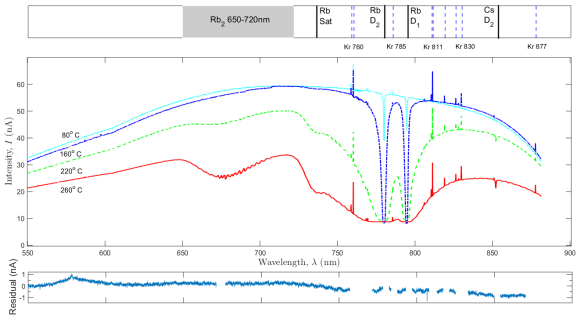

Figure 3: Monochromator spectrum at T=353 - 533 K and ^{4}He pressure of 10,000 Torr. Spectral features are assigned in the upper banner and the fit residuals for a 9^{th} order polynomial in regions without spectral structure is provided in the lower panel.

The transmitted intensity of Figure 3 is converted to absorbance, A, in Figure 4, using Beer's Law and the baseline spectrum from the cold scans as described above. The bottom panel in Figure 3 illustrates the residuals associated with the baseline polynomial fit to the data. In the regions with no atomic or molecular features, the residuals are unstructured with an average variance of ΔI = 1×10^{-9} A or approximately 2-5%. By examining the absorbance in the spectral region near the Rb D_2 and D_1 lines only, several new features are revealed. A slow saw-tooth cycling of temperature of 3 K (peak to valley) with a regular period of 3.5 minutes leads to a periodic variance in absorbance of up to ΔA = 0.02. This variance is fully removed by processing the data with the thermocouple readings,

as shown below. The absorbance due to the atmospheric O_2 $X^3\Sigma - b^1\Sigma(0,0)$ band near 762 nm is rotationally resolved. The absorbance of A=0.02 is consistent with a path length of 2 meters, largely within the monochromator. Additional detail from the Kr lamp is also evident in Figure 4.

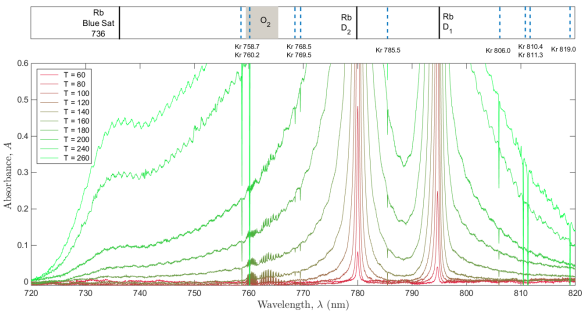

Figure 4: Absorbance spectra corresponding to the data in Figure 3. The magnetic dipole selection rules, Hunds case (b), produces four $O_2(b^1\Sigma \rightarrow X^3\Sigma)$ absorption branches: ${}^PP$ and ${}^PQ$, beginning near 762 nm and extending beyond 770 nm, and the ${}^RQ$ and ${}^RR$ lines from 762-759 nm.

At lower Rb densities, the core of the line shape is not opaque and the rates for collisional broadening, shifting and asymmetry may be evaluated. Figures 5 and 6 illustrates the observed line shapes for both the Rb D_2 and D_1 lines for ^{4}He and ^{3}He pressures of 500-15,000 Torr at 343 K. The D_1 lines exhibit a significant shift of the center frequency to the blue. In contrast, the D_2 lines exhibit a small blue shift. In all cases, the widths of the spectral features are 240-290 GHz at the highest pressure, depending on transition and buffer gas. The areas under these curves are nearly constant, varying by 18% for D_1 and 8% for D_2 due to modest changes in alkali density.

The Anderson-Talman theory for the line shape, limited to the low-pressure core of the line, can be expressed as two terms:

$$I(\nu) = 2\left(\frac{c}{\bar{\nu}}\right)e^{-n\alpha_0}\frac{\left[cos(n\beta_0)(n\alpha_1) + sin(n\beta_0)\left(\frac{2\pi c}{\bar{\nu}}\nu - n\beta_1\right)\right]}{(n\alpha_1)^2 + \left(\frac{2\pi c}{\bar{\nu}} - n\beta_1\right)^2} \quad (2)$$

where the first term is nearly Lorentzian at low perturber density, n, and represents the pressure broadened and shifted line core. The second term has a dispersive shape, with asymmetric shading. The rate for pressure broadening of the core Lorentzian, γ, is normally defined from the low pressure line shapes by the full-width half-maximum (FWHM) line width and expressed with units of MHz/Torr:

$$\Delta\nu_{FWHM} = \gamma P + \Delta\nu_n \quad (3)$$

where $\Delta\nu_n$ is natural broadening and

$$\gamma = \left(\frac{2\bar{\nu}}{\pi c}\right)\left(\frac{c}{kT}\right)\alpha_1 \quad (4)$$

Similarly, the rate for the pressure-induced shift of the line center is:

$$\delta = \left(\frac{2\bar{\nu}}{2\pi c}\right)\left(\frac{c}{kT}\right)\beta_1 \quad (5)$$

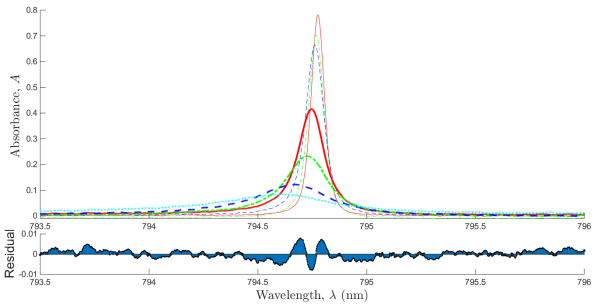

(a) D_1 ^{4}He

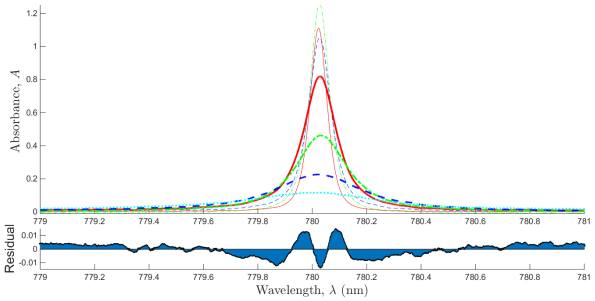

(b) D_2 ^{4}He

Figure 5: Core line shapes for (a) Rb D_1-^{4}He and (b) Rb D_2-^{4}He, at pressures from narrowest to widest of (—) 512 Torr, (–·–) 997 Torr, (- - -) 1,544 Torr, (...) 2,005 Torr, (——) 3,006 Torr, (—·—) 5,490 Torr, (– – –) 9,988 Torr, (•••) 15,039 Torr.

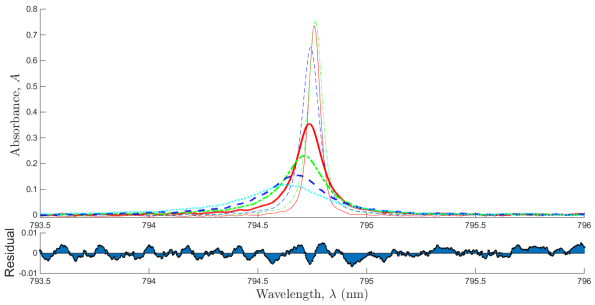

(a) D_1 ^{3}He

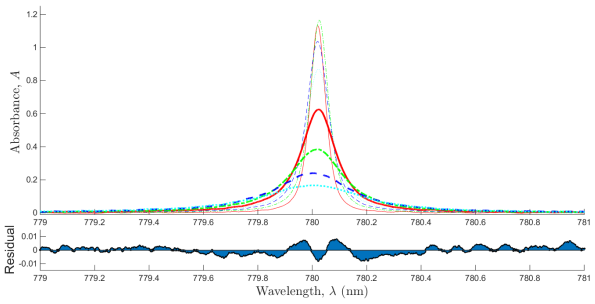

(b) D_2 ^{3}He

Figure 6: Core line shapes for (a) Rb D_1-^{3}He and (b) Rb D_2-^{3}He, at pressures from narrowest to widest of (—) 502 Torr, (–·–) 998 Torr, (- - -) 1,498 Torr, (...) 1,994 Torr, (——) 3,015 Torr, (—·—) 5,001 Torr, (– – –) 7,500 Torr, (•••) 10,062 Torr.

Finally, the asymmetry of the line shape, or how much of a tail the line shape has to one side compared to the other, is described by the parameter, β_o.

A fit of equation (2) to the full set of data for T = 343 K similar to that provided in Figures 5 and 6 yields the rate parameters reported in Table 1. The fits are limited to the core of the line, defined as the signal near resonance from 25% of the peak to the peak. The wing of the lines and secondary maximum are not described by equation 2 and are discussed further below. The quality of the fits is indicated by the residuals displayed in Figures 5 and 6. Typically, 8 spectra were recorded at pressures of 50-15,000 Torr. Linear fits yield the rates in Table 1 with uncertainties reported as the 95% confidence interval. The statistical errors reported in Table 1 are similar to the instrumental line shape and spectral calibration errors of ≈0.17 MHz/Torr, as specified above.

The prior experimental ^{4}He broadening rates for the D_2 line vary from 14.3-22.5 MHz/Torr and were measured in a modest temperature range of 310-394 K. The modern results (since 1990) are more closely grouped with an average of 18.8 ± 1.7 MHz/Torr. Scaling the rates to a common temperature requires a prediction of the temperature dependent cross-section, (51; 20; 41; 43) but only marginally reduces the variation in the results. The current observation is somewhat lower at 17.0 ± 0.3 MHz/Torr, just outside of the range of the modern measurements. The modern D_1 rates exhibit a smaller range with an average of 18.2 ± 0.6 MHz/Torr, and the present result is again somewhat low. The grating spectrometer employed in the current work is designed to examine the far wings of the lineshapes and has poorer spectral resolution than the laser absorption experiments. The preferred results are from references (45; 44; 51).

It is worth noting that the theoretical predictions for the D_1 broadening rate, even when using the same interaction potentials and temperature, vary from 15.7-20.2 MHz/Torr. The semi-classical Anderson-Tallman line shape theory predictions (9) and the full quantum mechanical Baranger calculations done by Loper (33) yield predictions that vary by more than the range of experimental observations. The Anderson-Talman theory for the full line shape is discussed in Section 4.3.

Comparing the ^{4}He and ^{3}He results reveals an interesting trend. For the D_2 line the current ^{3}He rate is 4% larger than the ^{4}He rate, which agrees almost exactly with the only prior study of both collision partners (44). Similarly for the D_1 line, the ratio is 14% higher in the current results, compared with 15% in reference (44). The primary isotope effect is the higher relative speed of the collision pair, which would predict a 15% increase for ^{3}He due to the reduced mass of the ^{3}He.

The collision induced shift rates are dramatically higher for the D_1 line than the D_2 line. The D_2 line is influenced by two surfaces, with competing binding (see Section 4.2), yielding small shifts. The current result for the D_1 line, 4.60 ± 0.12 MHz/Torr and 5.65 ± 0.35 MHz/Torr for ^{4}He and ^{3}He respectively, agree quite favorably with the prior modern results with averages of 4.6 ± 0.2 MHz/Torr and 5.8 ± 0.5 MHz/Torr. The agreement for the D_2 line is similar with the present results of 0.2 ± 0.14 MHz/Torr and 0.65 ± 0.2 MHz/Torr in agreement

Table 1: Pressure Broadening and Shift Rates
In the table of rates below the Broadening (γ) and Shift (δ) rates are given in MHz/Torr with Asymmetry (β) parameter reported as rad nm^3

	D1	D2	Temp	Ref
^{4}He γ	16.1 ± 0.2	17.0 ± 0.3	343	Exp
	17.6 ± 0.1	16.5 ± 0.1	353	(42)
		20.3 ± .3	314	(51)
	18.9 ± 0.2	20.0 ± 0.2	394	(45)
	18.3 ± 0.2	18.4 ± 0.2	353	(44)
	17.9 ± 0.2		373	(34)
	19.0 ± 2.0	15.0 ± 2.0	320	(23)
	18.3 ± 0.9			(25)
		22.5 ± 1.1	310	(6)
	18.5 ± 3.4	18.5 ± 3.4	320	(40)
	19.3	18.1	313	Theory
	21.6	19.8	394	(9)
	15.7	21.3	394	(33)
	14.3	14.3	320	(26)
	17.1	12.5	450	(46)
^{4}He δ	4.60 ± .12	.20 ± .14	343	Exp
	4.57 ± .02	0.28 ± .05	353	(42)
		0.39 ± .06	314	(51)
	4.71 ± .04	0.37 ± .06	394	(45)
	4.40 ± 0.1	.47 ± .06	353	(44)
	5.0 ± 1.0	0.9 ± 0.2	320	(23)
	6.2 ± 0.5			(25)
		2.2 ± 0.5	310	(6)
		-0.74 ± 0.34	320	(40)
	4.66	0.20	393	Theory
	5.8	1.10	394	(9)
	-5.8	-1.13	394	(33)
	1.09	1.09	320	(26)
	4.13	1.76	450	(46)
^{4}He β_0	0.51 ± .04	0.24 ± .02	343	Exp
	-0.98 ± 0.03	-0.12 ± 0.03	353	(44)
	-0.61 ± 0.03	-0.14 ± 0.04	353	(42)
	1.1	0.3	313	Theory
^{3}He γ	16.8 ± 0.5	19.4 ± 0.4	343	Exp
	19.0 ± 0.3	21.2 ± 0.2	353	(44)
	18.12 ± 0.07	20.30 ± 0.08	363	(27)
	26.32		393	(32)
	19.6	20.1	393	Theory
^{3}He δ	5.65 ± 0.35	0.65 ± 0.2	343	Exp
	5.4 ± .05	.62 ± .04	363	(27)
	6.32		393	(32)
	5.74 ± 0.15	0.69 ± 0.05	353	(44)
	5.45	-0.01	393	Theory
^{3}He β_0	0.43 ± 0.01	0.30 ± 0.03	343	Exp
	-0.55 ± 0.03	-0.24 ± 0.03	353	(44)
	0.50	0.125	333	Theory

with the average prior results of 0.38 ± 0.08 MHz/Torr and 0.65 ± 0.04 MHz/Torr. However, the theoretical predictions sometimes disagree even on the sign of the shift.

In Figure 7, the spectra are folded about the line center to illustrate the asymmetric nature of the modified Lorentzian line shape. The asymmetry parameter, β_o, is positive, reflecting a higher intensity on the blue side of the line, consistent with equation (2). The asymmetry is somewhat larger for the D_1 line and has the same sign as the shifting rate. The asymmetry rates generally follow the trends observed for the collision induced shifts, as previously reported for Csrare gas collisions (8). The asymmetry parameters from prior studies reported in Table 1 use a different sign convention, where $\beta_o < 0$ implies a repulsive interaction potential (44). The current and prior observed line shapes for He all exhibit a higher intensity on the blue side of the line.

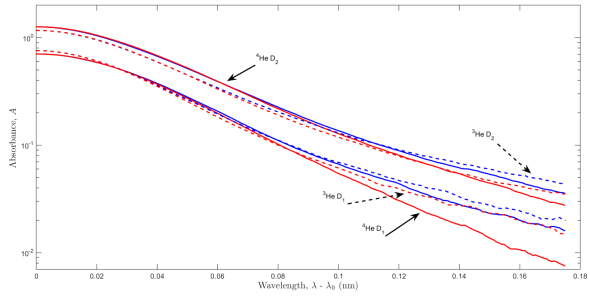

Figure 7: Asymmetric line shapes observed at 343 K and 998 Torr for (—) ^4He and (- - -) ^3He. The red wings (—) are less intense than the blue wings (—) of the line shape, yielding a positive value for β_0

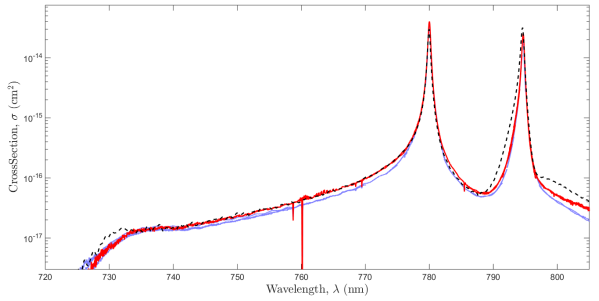

Figure 8: Absorption cross-sections at 10,000 Torr observed for: (—) ^{4}He and (—) ^{3}He and (- - -) predicted from the Anderson-Talman theory with dipole moment variation and absorption Boltzmann factor. The spectra are obtained by merging the observed absorbance at T = 333 K near line center to T = 533 K in the far wings. The oxygen absorption and several calibration lamp lines are retained in the ^{3}He spectrum.

The primary focus of the current work is to characterize the high pressure line shapes, focusing on the non-Lorentzian features far from line center. In particular, the broader absorption spectrum of Figure 4 illustrates the blue satellite of the D_2 line near 735 nm. The location, height and shape of this satellite peak is a strong probe of the interaction potential. To better characterize the full line shape, the absorbance is converted to the cross-section in Figure 8. The absorption cross-section, σ, is defined as:

$$\sigma(\lambda) = A/(nL) = \frac{g_u}{g_l}\frac{\lambda^2}{8\pi}A_{ul}g(\lambda) \quad (6)$$

where

n = Rb density

L = vapor path length = 8.125 cm

$g_{u,l}$ = degeneracy of the upper and lower levels: $g(^2P_{3/2}) = 4$, $g(^2S_{1/2}) = g(^2P_{1/2}) = 2$

A_{ul} = spontaneous emission rate between the upper and lower level: $A(^2P_{3/2}) = 3.81x10^7 s^{-1}$ and $A(^2P_{1/2}) = 3.61x10^7 s^{-1}$

$g(\lambda)$ = the wavelength dependent transition line shape

For a Lorentzian line shape with a width of 170 GHz (the D_2 line at 10,000 Torr), the peak cross-section would be $\sigma = 6.9x10^{-14}\ cm^2$, about twice the value observed in the spectrum of Figure 8 with a peak D_2 cross-section of $3.6x10^{-14}\ cm^2$. The Rb density appears to be overestimated by the wall temperature, with ΔT = 6K sufficient to explain the difference.

The variation in Rb density due to cycling of the temperature control loop produces a periodic variance in the absorbance of Figure 4. This variation is removed in Figure 8. The temperature varies periodically with a peak-to valley difference of 3 K and a period of 3.5 min. At T= 473 K, the Rb vapor pressure curve exhibits a 12% change in density for the 3 K temperature variation. By ratioing the observed absorbance to the Rb density when calculating the absorption cross-section, this variance is fully removed.

The absorption cross section reported in Figure 8 is comprised of absorbance spectra for six Rb densities, $n = 2.35 \times 10^9 - 5.36 \times 10^{13} atoms/cm^3$ (T = 333-533 K). By merging the absorbance at low density for the line center and at high density for the blue satellite, a single curve is developed with larger dynamic range. A variation in cross-section of more than 4 orders of magnitude is observed. Note that the shapes of the ^4He and ^3He wing spectra are quite similar. The location of the D_2 blue satellite is 735.7 nm independent of pressure with an amplitude of 0.03% of the peak at T= 100^oC and 10,000 Torr. The location of the blue satellite is predicted by the maximum in the X-B difference potential as discussed below at 728.6 nm. The B barrier in the $B^2\Sigma^+_{1/2} - X^2\Sigma^+_{1/2}$ difference potential from reference (12) predicts the He blue satellite at 721.5 nm, whereas the surfaces reported in reference (10) predict a maximum at 723.8 nm. The current ab initio surfaces systematically over predicted the barrier height in the $B^2\Sigma^+_{1/2}$ surface.

4. Discussion and predicted line shapes

The observed high-pressure line shapes are compared with predictions of the semi-classical Anderson Talman theory in the following discussion. The presentation includes a brief development of the theory, a description of the potential surfaces, and a comparison of the predictions with the current observations.

4.1. Anderson Talman Line shape theory with dipole moment variation

In the Anderson Talman theory of pressure broadening, (40) the line shape, $I(\nu)$, is determined from the Fourier transform of the auto-correlation function, Φ:

$$I(\nu) \propto Re \int_0^\infty \Phi(s) e^{i2\pi\nu s} ds \tag{7}$$

$$\Phi(s) = e^{-ng(s)} \tag{8}$$

where n is the density of the perturber and the accumulated phase difference, g(s), is defined by the difference potential, ΔV(r), and collision trajectory with impact parameter, b, and relative speed, v. We have recently applied this theory to the Cs D_1 and D_2 lines for collisions with rare gases and the approach is developed in further detail in reference (20). Recently, Allard et. al. (1) has derived a modified version of the Anderson-Talman equations that incorporates the variation of dipole transition moments, d, with inter-nuclear separation, r. They also include a Boltzmann term that gives the probability distribution for inter-nuclear separation,

$$\bar{d}(r) = d(r) e^{V_X(r)/2kT} \tag{9}$$

where V_X is the ground state surface used to describe an absorption profile. With these modifications, the accumulated phase for a single adiabatic surface is:

$$g(s) = \frac{1}{\bar{d}^2(r(0))} \int_0^\infty 2\pi b db \int_\infty^\infty \left[\bar{d}^2(r(0)) - Exp\left(\frac{-i}{\hbar} \int_0^s dt \Delta V(r(t)) \right) \bar{d}(r(0)) \bar{d}(r(s)) \right] dx \tag{10}$$

assuming straight line trajectories:

$$r(t) = \sqrt{b^2 + (x + \bar{v}t)^2} \tag{11}$$

Allard et. al. note that including the Boltzmann factor is not consistent with straight line trajectories, but improves agreement with experiment (1). Equation (10) uses an average velocity, $\bar{v}$, rather than including the Maxwellian speed distribution. With this form of the difference potential, the integral over time, t, in the exponential can be accomplished analytically. The remaining two integrals over x and b are accomplished numerically.

The real and imaginary parts of the accumulated phase

$$g(s) = \alpha + i\beta \tag{12}$$

at large correlation distances, s, become linear:

$$\alpha(s) = \alpha_0 + \alpha_1 s \tag{13}$$

$$\beta(s) = \beta(0) + \beta_1 s \tag{14}$$

yielding the core line shape of Equation (3.2). The wing of the line shape requires the full integral analysis of Equations (3.7-11).

4.2. Potential surfaces

The diatomic potential surfaces that arise for collisions between the rubidium in its ground $^2S_{1/2}$ state or first excited $^2P_{1/2,3/2}$ states, and helium are required to predict the D_1 and D_2 line shapes. The ground $X^2\Sigma^+_{1/2}$ and excited $A^2\Pi_{1/2}$, $A^2\Pi_{3/2}$ and $B^2\Pi^+_{1/2}$ potential energy surfaces have been calculated using one-electron pseudopotential technique and are provided in Figure 9.

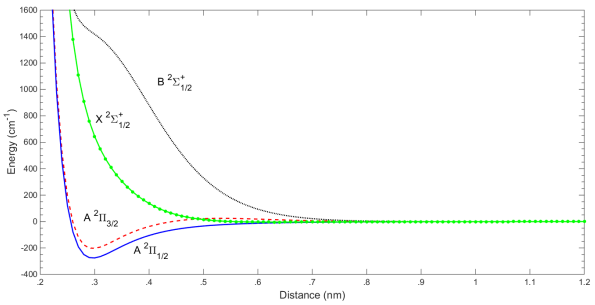

Figure 9: Rb-He potential energy surfaces

The calculation method is based on the use of pseudopotentials, which reduces the Rb-He excimer to a one-electron molecular problem. In this model, Rb^+ and He are treated as two closed-shell cores interacting with the alkali valence electron via semi-local pseudopotentials. The total potential energy includes the core-core interaction, the interaction between the Rb valence electron and the ionic system Rb^+-He, and the spin orbit coupling.

The core-core interaction, which corresponds to the Rb^+-He ground state potential energy curve, is taken from the accurate coupled cluster calculations of Hickling et al. (21) Single and double excitations were included, along with a perturbative treatment of the triple excitation terms, CCSD(T). This potential is fit using the analytical form of Tang and Toennies (48). The equilibrium distance of the neutral dimer is larger than that of the ionic system, and few energies were calculated around this distance. Providing an analytical form for the Rb^+-He core-core interactions increases the accuracy in the region of interest for the neutral Rb-He dimer. The analytical form contains the well-known long range van der Waals terms and an exponential short-range repulsion. By least squares fitting, the parameters of the analytical form were derived. An excellent agreement is observed between the analytical and the original numerical potential. The difference between the analytical and the numerical potentials for all internuclear distances is $< 3\ cm^{-1}$.

For the interaction between the Rb valence electron and the ionic system, Rb^+-He, we have performed a one-electron ab initio calculation using semi-local pseudopotential for the Rb^+ core and the electron-He effects. The electron-He atom interaction was represented by a pseudopotential fitted in our group. However, the Rb atom has been represented by the one-electron pseudopotential proposed by Barthelat et al. (18) and used in previous calculations (7; 15; 16). In addition, we take into account the core-valence correlation by applying the operator formulated by Müller et al. (38). For each atom (Rb or He), the

core polarization effects are described by the effective potential proposed by Müller and Meyer. The electric dipole polarizabilities were taken as 9.245 a.u. for the Rb^+ core and 1.3838 a.u. for He (50; 31).

The pseudopotential parameters were optimized in order to reproduce the ionization potentials and the lowest valence s, p and d one-electron states as deduced from the atomic data tables. The Gaussian type orbital basis sets used for the rubidium and helium atoms were 6s/6p/4d and 3s/3p. The calculated ionization potential and the lowest atomic energy levels for Rb were compared with the experimental data (5; 37) and a good agreement was observed. The largest absolute error is 32.43 cm^{-1} obtained for 5s-6p transition energy.

The spin-orbit interaction is evaluated using the semi-empirical scheme of Cohen and Schneider (14). The spin-orbit coupling for the electronic states, dissociating into 5p, is given by the following matrix:

$$\begin{bmatrix} E_p\left(^2\Pi\right) - 1/2\xi & \xi/\sqrt{2} & 0 \\ \xi/\sqrt{2} & E_p\left(^2\Sigma^+\right) & 0 \\ 0 & 0 & E_p\left(^2\Pi\right) + 1/2\xi \end{bmatrix} \quad (15)$$

The diagonalization of such a matrix provides us with the eigenvalues and the energy splitting leading to three molecular states related to the atomic limits $S_{1/2}$, $P_{1/2}$ and $P_{3/2}$. The spin orbit coupling constant ϵ_{5p} (Rb) = 158.396 cm^{-1} was used in the present calculation. The rotation matrix issued from the diagonalization is used to determine the dipole moment including the spin-orbit interaction.

The atomic asymptotic limits in Figure 9 have been shifted to E=0 to better compare the surfaces. The ground $X^2\Sigma^+_{1/2}$ surface correlating with Rb 5 $^2S_{1/2}$ is largely repulsive with a very shallow well of depth ≈ 4 cm^{-1} at about 0.63 nm. The $A^2\Pi_{1/2}$ surface correlating with Rb 5 $^2P_{1/2}$ has a well of 202.9 cm^{-1} near 0.30 nm. A local maximum of 24.3 cm^{-1} occurs at longer range, near 0.53 nm. The $A^2\Pi_{3/2}$ and $B^2\Sigma^+_{1/2}$ both correlate to Rb 5 $^2P_{3/2}$. The $A^2\Pi_{3/2}$ well is deeper than the $A^2\Pi_{1/2}$ surface , 275 cm^{-1}, but at the same location, 0.30 nm. The $B^2\Sigma^+_{1/2}$ exhibits a long range shallow well of 0.85 cm^{-1} near 1.0 nm. The barrier appears as a broad shoulder near 0.35 nm, with no minimum at shorter range. These well depths differ by those reported in reference (10) by 20-210%.

The corresponding difference potentials are shown in Figure 10. There is no long range minimum in the $A^2\Pi_{3/2}$-$X^2\Sigma^+_{1/2}$ difference potential and the minimum for $A^2\Pi_{1/2}$-$X^2\Sigma^+_{1/2}$ is less than 0.2 cm^{-1} suggesting no red satellite features for the D_1 and D_2 lines. The D_1 $A^2\Pi_{1/2}$-$X^2\Sigma^+_{1/2}$ difference potential has a positive extremum of 24.4 cm^{-1} at a separation of 0.57 nm. The $B^2\Sigma^+_{1/2}$-$X^2\Sigma^+_{1/2}$ component of the D_2 transition has a positive extremum of 907.7 cm^{-1} at a separation of 0.34 nm. The variation of dipole moment with nuclear separation and the Boltzmann factors described in equations (9-10) are provided for each surface in Figure 11. The dipole moments for the current B-X surface decrease from the asymptotic limit by < 15% at r = 3 nm, with minimal variation for the other transitions. The variation at shorter distances has minimal impact on the line shapes. However, the Boltzmann factors vary by a factor of 2-3 for the X and B states, and will significantly modify the wing line shapes.

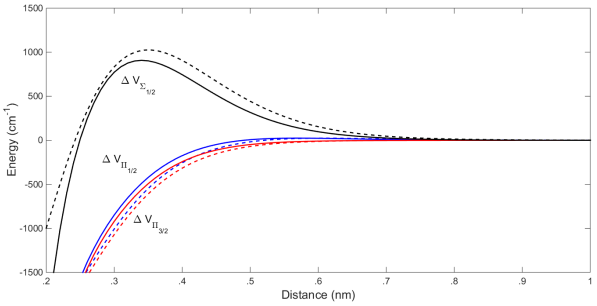

Figure 10: Rb-He difference potentials for the current work (—) and (- - -) for the identical potentials used by Blank (10) and Bouhadjar (12).

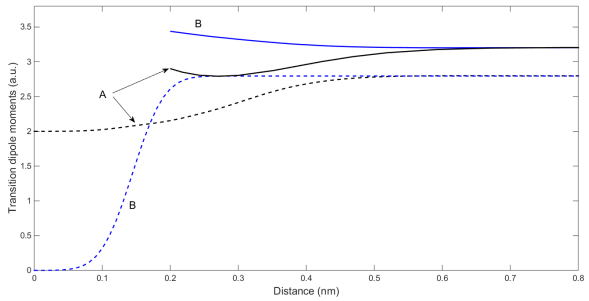

(a)

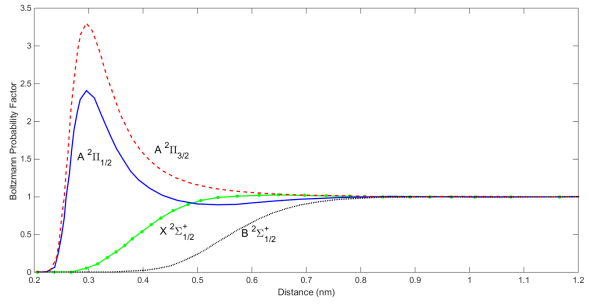

(b)

Figure 11: Dipole moment (a) and Boltzmann Factors (b). Hager (- - -) (20) and Bouhadjar (—) (12). A corresponds to the dipole moment for the $X - A$ transitions with B corresponding to the $X - B$ transition.

To compute the D_1 and D_2 spectra we treat each of the difference potentials separately. The D_1 line is separated from the D_2 line in Rb by 237 cm^{-1} and only the $X - A^2\Pi_{1/2}$ difference potential is required to compute the line shape. The D_2 line is more complicated and requires both the $X - A^2\Pi_{3/2}$ and X-B difference potentials. An approximate method to treat this problem for large spin orbit coupling is to compute $g(s)$, for each difference potential and weight them equally to compute the correlation function. This procedure is equivalent to a convolution of the two spectral lines. For ease of computation, we

fit the numerical difference potentials to an expansion in $1/r^n$, with n = 6-20.

In our recent work on Cs rare gas line shapes, several empirical modifications of the potential surfaces were required to achieve reasonable agreement with the observed line shapes (20). No empirical modifications of the potential surfaces are required in the present study.

4.3. Comparison of observed and predicted line shapes

The broadening, shifting and asymmetry parameters as predicted by Equation (3.2) are compared with the present observations in Table 1. The calculated broadening rates are systematically larger than the currently observed rates by 1.1-3.2 MHz/Torr and agree within 20%. The ^{3}He broadening rates are higher due to the increased relative velocity. However, the increase is not as high as anticipated and different for the D_1 and D_2 lines due to a line dependent decrease in cross-section with temperature, as discussed below. The collision induced shift rates are generally more sensitive to interaction potential and yet exhibit very good agreement.

There is a significant difference in the shift rates for the D_1 and D_2 lines. This has also been observed in our recent Cs study (20). The $A^2\Pi_{3/2}$-$X^2\Sigma^+_{1/2}$ difference potential yields red shifts, whereas the long-range barrier in the $B^2\Sigma^+_{1/2}$-$X^2\Sigma^+_{1/2}$ surfaces yields a blue shift. The convolution of these two line shapes yields a smaller blue shift for the He D_2 line. In contrast, the D_1 line involves only the $A^2\Pi_{1/2}$-$X^2\Sigma^+_{1/2}$ surface which exhibits a modest barrier and thus a larger blue shift. The magnitude of the predicted shift rate is about twice the measured value for the D_1 line, but close to the small value observed for the D_2 line. The predicted shifts rates are remarkably similar to the observations, except for the ^{3}He D_2 line. Indeed, the predictions for the ^{3}He D_2 line suggest a near zero shift, whereas the observations indicate an increased shift to the blue. The temperature dependence of the cross-section for the D_2 shift appears to be a most sensitive probe of the interaction potential, and is discussed further below. The predicted asymmetry parameters are correlated with the shift rates.

Several predictions of the high pressure D_1 and D_2 line shapes for Rb-^{4}He and ^{3}He collision pairs, at 10,000 Torr and T = 333 K near line center and T = 533 K in the far wings, are provided in Figure 12. Each spectrum consisting of 105 digitized points was computed numerically from the Fourier transform of the correlation functions for the D_1 and the convolved D_2 difference potentials.

The blue satellite predicted for the D_2 line is readily apparent and located at 735.7 nm, consistent with the observations of Figure 4. This secondary maximum in the D_2 far blue wing occurs at a wavelength corresponding to the barrier height in the $B-X$ difference potential. The barrier of 907.7 cm^{-1} reported in Figure 10 leads to the observed shift of 52 nm. The extremum in the difference potential is broader and occurs at shorter range for Rb than the corresponding surfaces for Cs. This is consistent with the stronger, more defined blue satellite in Cs (20). Inclusion of the variation in dipole moment and corresponding Boltzmann factors in equations (9-10) further flattens and re-

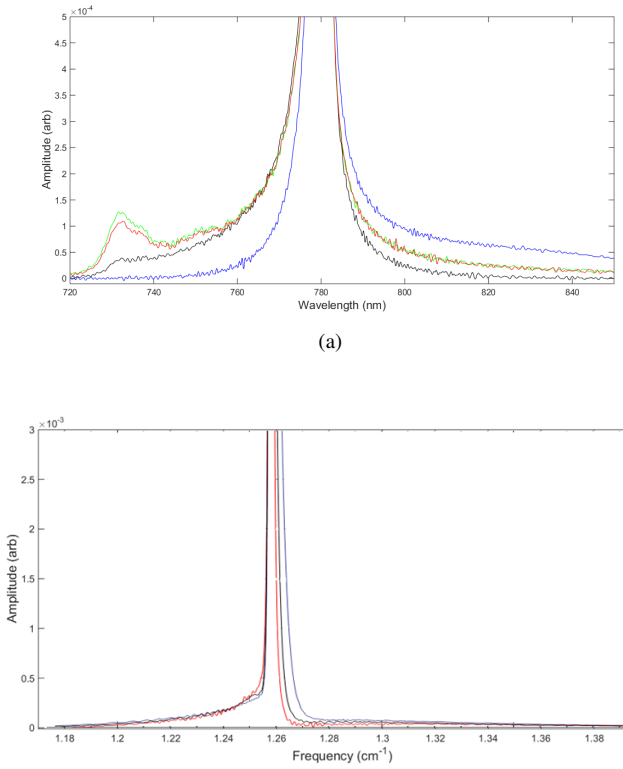

(a)

(b)

Figure 12: Predicted ^{4}He line shapes at 10,000 Torr and 333K: (a) Rb D_2 line with convolution of both surfaces, assuming from top to bottom (—) no dipole moment variation, (—) dipole moment variation with no Boltzmann factor, (—) dipole moment variation with ground state Boltzmann factor, and (—) dipole moment variation with excited B state Boltzmann factor; (b) Rb D_1 line with (—) unmodified potentials, (—) difference potential scaled by 0.5, and (—) difference potential scaled by 2.0.

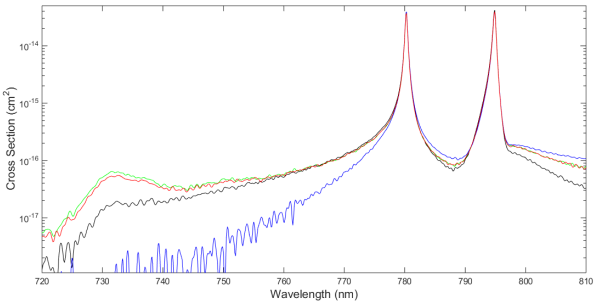

(a)

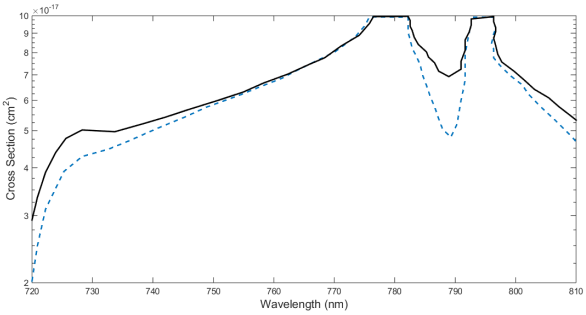

(b)

Figure 13: (a) Predicted full scan of absorption cross-section on logarithmic scale, and (b) absorption cross-section from Bouhadjar (12) at 320 K (- - -) and 500 K (—).

duces the magnitude of the peak of the blue satellite. The variation in dipole moment has a minor effect on the amplitude of the blue satellite. The effect of the Boltzmann factor in absorption (using the ground state potential) is more significant and produces a blue satellite with a poorly defined peak and agrees well with the current observations. A Boltzmann factor based on the B state surface, as suggested for emission (1), dramatically reduces the intensity of the far wing, inconsistent with the observed line shape.

The D_1 line shown in Figure 12 exhibits a red shoulder, which may result from the tail of a strong, but unresolved, blue feature that is blended with the core. The barrier heights for the $A^2\Pi_{1/2}$-$X^2\Sigma^+_{1/2}$ transitions are considerably less, leading to smaller shifts and larger amplitudes. The D_1 blue satellite is about $0.5x10^{-3}$ of the resonant peak, or ≈5 times larger than the D_2 blue satellite. The blue D_1 satellite does not present a spectral peak, but rather generates a shoulder on the core line shape.

A full prediction of the Rb-^{4}He line shape for both lines is directly compared with the experimental results in Figure 8. The potentials of Figure 9 do not require empirical modification to provide excellent quantitative agreement. The dipole moment variation and absorption Boltzmann factor is critical to obtaining strong agreement. The difference in the modeled and predicted D_1 line is the greatest. The experimental observations for the ^{3}He and ^{4}He collision partners also exhibit a greater difference on the red side of the D_1 line, presumably reflecting greater temperature dependence.

4.4. Predictions of the temperature dependent broadening and shifting rates

A prediction for the temperature dependence of the broadening and shifting rates is provided in Figure 9. The rates are converted to cross-sections:

$$\sigma_b = \gamma\left(\frac{kT}{\bar{v}}\right) \tag{16}$$

$$\sigma_s = \delta\left(\frac{kT}{\bar{v}}\right) \tag{17}$$

to remove the influence of relative velocity on the results. Two sets of predictions are provided for each case. Using the average velocity as expressed in Equation 3.10 allows for highly sampled temperature dependence. However, non-physical oscillations are observed, particularly for the D_2 line. By employing a Maxwellian distribution of relative speeds the oscillations are removed, but the temperature dependence is less sampled, due to the increased numerical complexity.

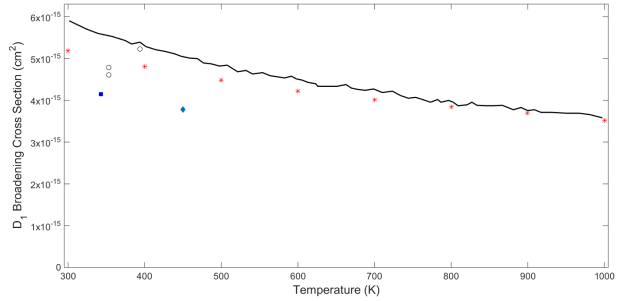

(a)

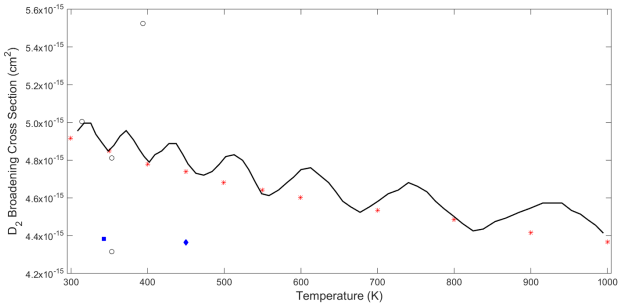

(b)

Figure 14: Predicted temperature dependence for the broadening cross-sections for the Rb-^{4}He D_1 and D_2 lines using: (—) average velocity and (*) full Maxwellian speed distribution. Experimental observations for: (□) ^{4}He, (⋄) ^3He with mass change reflected as temperature increase, and (○) prior observations from references (42; 44; 45; 51).

Often, broadening cross-sections are assumed independent of temperature, as predicted for a hard sphere interaction. Alternatively, the broadening cross-section for a long range attractive, r^{-6}, interaction, yields a $T^{-0.3}$ dependence (22; 51). The D_2 broadening cross-section is nearly independent of temperature, whereas the D_1 line is closer to the predicted van der Waals potential, presumably due to the single, isolated surface. Note that

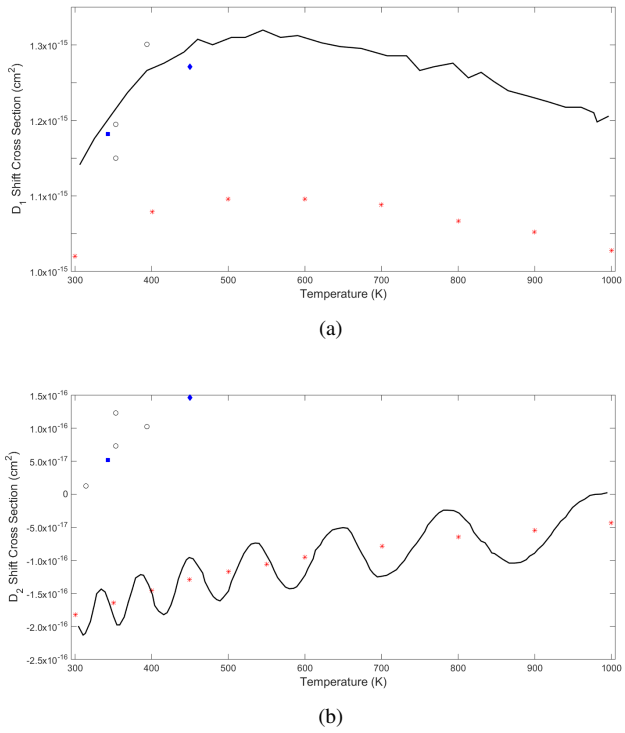

Figure 15: Predicted temperature dependence for the shifting cross-sections for the Rb-^{4}He D_1 and D_2 lines using: (—) average velocity and (*) full Maxwellian speed distribution. Experimental observations for: (□) ^{4}He, (⋄) ^{3}He with mass change reflected as temperature increase, and (∘) prior observations from references (42; 44; 45; 51).

the shallower well observed for the Rb-He system compared with Cs-Ar with higher polarizability, (20) produces a smaller temperature dependence. The ^{3}He collision partner is a reasonable substitute for higher temperature conditions, as the potential surfaces are unchanged. The observed ^{3}He broadening rate does not increase as much as predicted by the mass effect on average velocity. This difference is greater for the D_1 line, consistent with the predicted stronger temperature dependence of the cross-section. The predicted isotope effect on the D_2 shift rate is less supported by the data. At high temperatures the predicted shift rate trends toward zero, whereas the observed rate increases to the blue. The shift rate is more sensitive to the interaction potential and the weighting of the two surfaces. A detailed experimental study of the temperature dependence requires the development of an alkali vapor cell where the temperature can be increased without modifying the alkali vapor density. In the current apparatus, temperature controls the Rb vapor pressure and the line center quickly becomes opaque at T $>$ 373 K.

The cross-sections for collision-induced shifts depend critically on the interaction potentials. For the rather large blue shift associated with the D_1 line, the shift cross-section is predicted to depend only weakly on temperature. However the small shift predicted for the convolved D_2 line approaches zero at high temperature.

Given the experimental fidelity available in experimentally observed line shifts from laser absorption experiments of about 1% error, an experimental test of the current predictions is warranted, but requires independent control of Rb vapor density and gas temperature. Unfortunately, the available experimental results span a small range of temperatures and have been measured with different techniques.

5. Conclusions

The experimentally observed, non-Lorentzian line shapes for the Rb D_1 and D_2 lines broadened by ^{4}He and ^{3}He at pressures up to 20 atmospheres (≈15,000 Torr) are in strong quantitative agreement with the predictions of the Anderson-Talman theory using one electron pseudo potentials. The predictions of the line core broadening agree with the observations to within 14%. The agreement for shifting rates is better, 10%, except for the ^{3}He D_2 line which is near zero. The significant difference in the observed shift rates for the D_1 and D_2 lines is explained by the convolution of the red shifted line shape from $A^2\Pi_{3/2} - X^2\Sigma^+_{1/2}$ difference potential with the blue shifted line shape of the $B^2\Sigma^+_{1/2} - X^2\Sigma^+_{1/2}$ surface. The asymmetry parameters predictions are less accurate, with more than a factor of two disagreements with observations. To match the location, amplitude and shape of the blue wing of the D_2 line requires the inclusion of dipole moment variation and Boltzmann factor. The difference in the modeled and observed wings of the D_1 line is larger, including a significant difference for ^{3}He and ^{4}He collision, suggesting a more sensitive dependence on temperature. The current prediction for the temperature dependence of the line shape parameters awaits an experimental verification at low Rb density.

6. Acknowledgments

This work was supported in part by a Window on Science grant from the Air Force Office of Scientific Research.

[1] Allard, NF, A Royer, JF Kielkopf, and N Feautrier. “Effect of the variation of electric-dipole moments on the shape of pressure-broadened atomic spectral lines”. *Physical Review A*, 60(2):1021, 1999.

[2] Allard, NF and F Spiegelman. “Collisional line profiles of rubidium and cesium perturbed by helium and molecular hydrogen”. *Astronomy & Astrophysics*, 452(1):351–356, 2006.

[3] Allard, Nicole and John Kielkopf. “The effect of neutral nonresonant collisions on atomic spectral lines”. *Reviews of Modern Physics*, 54:1103–1182, Oct 1982. URL `http://link.aps.org/doi/10.1103/RevModPhys.54.1103`.

[4] Anderson, PW and JD Talman. “Pressure broadening of spectral lines at general pressures”. *Bell System Technical Publication*, 3117, 1956.

[5] Arnold, E, W Borchers, HT Duong, P Juncar, J Lerme, Peter Lievens, W Neu, R Neugart, M Pellarin, J Pinard, et al. “Optical laser spectroscopy and hyperfine structure investigation of the 102S, 112S, 82D, and 92D excited levels in francium”. *Journal of Physics B: Atomic, Molecular and Optical Physics*, 23(20):3511, 1990.

[6] Belov, VN. “Measurement of the constants for the broadening and shift of the D$_2$ line of rubidium (780.0 nm) by inert gases”. *Optics and Spectroscopy*, 51:209–211, 1981.

[7] Berriche, Hamid. “Electronic, spectra, and spin orbit interaction for FrAr van der Waals system”. *International Journal of Quantum Chemistry*, 113(9):1349–1357, 2013.

[8] Blank, Aaron L. *Potential Energy Curves and Associated Line Shape of Alkali-Metal and Noble-Gas Interactions*. PhD Dissertation, Air Force Institute of Technology, 2014.

[9] Blank, L and David E Weeks. "Impact broadening, shifting, and asymmetry of the D_1 and D_2 lines of alkali-metal atoms colliding with noble-gas atoms". *Physical Review A*, 90(2):022510, 2014.

[10] Blank, L, David E Weeks, and Gary S Kedziora. "M + Ng potential energy curves including spin-orbit coupling for M = K, Rb, Cs and Ng = He, Ne, Ar". *The Journal of Chemical Physics*, 136(12):124315, 2012.

[11] Bogachev, A V, Sergey G Garanin, A M Dudov, V A Eroshenko, S M Kulikov, G T Mikaelian, V A Panarin, V O Pautov, A V Rus, and Stanislav A Sukharev. "Diode-pumped caesium vapour laser with closed-cycle laser-active medium circulation". *Quantum Electronics*, 42(2):95, 2012.

[12] Bouhadjar, F, K Alioua, MT Bouazza, and M Bouledroua. "Rubidium D1 and D2 atomic lines pressure broadened by ground-state helium atoms". *Journal of Physics B: Atomic, Molecular and Optical Physics*, 47(18):185201, 2014.

[13] Carrington, C Gerald and Alan Gallagher. "Blue satellite bands of Rb broadened by noble gases". *Physical Review A*, 10(5):1464, 1974.

[14] Cohen, James S and Barry Schneider. "Ground and excited states of Ne2 and $Ne2^+$. I. Potential curves with and without spin-orbit coupling". *The Journal of Chemical Physics*, 61(8):3230–3239, 1974.

[15] Dhiflaoui, J and H Berriche. "One-Electron Pseudopotential Investigation of CsAr van der Waals System Including the Spin- Orbit Interaction". *The Journal of Physical Chemistry A*, 114(26):7139–7145, 2010.

[16] Dhiflaoui, J, H Berriche, M Herbane, AG AlSehimi, and MC Heaven. "Electronic Structure and Spectra of the RbAr van der Waals System Including Spin–Orbit Interaction". *The Journal of Physical Chemistry A*, 116(43):10589–10596, 2012.

[17] Drummond, DL and Alan Gallagher. "Potentials and continuum spectra of Rb-noble gas molecules". *The Journal of Chemical Physics*, 60(9):3426–3435, 1974.

[18] Durand, Philippe and Jean-Claude Barthelat. "A theoretical method to determine atomic pseudopotentials for electronic structure calculations of molecules and solids". *Theoretica chimica acta*, 38(4):283–302, 1975.

[19] Granier, J and R Granier. "Temperature effect on the displacement and broadening of the resonance lines of rubidium excited by argon". 1966.

[20] Hager, Gordon D, Gordon E Lott, Aaron J Archibald, L Blank, David E Weeks, and Glen P Perram. "High pressure line shapes for Cs D_1 and D_2 lines and empirically informed interaction potentials". *Journal of Quantitative Spectroscopy and Radiative Transfer*, 147:261–273, 2014.

[21] Hickling, Holly L, Larry A Viehland, Dessa T Shepherd, Pavel Soldán, Edmond PF Lee, and Timothy G Wright. "Spectroscopy of M^+·Rg and transport coefficients of M^+ in Rg (M = Rb–Fr; Rg = He–Rn)". *Physical Chemistry Chemical Physics*, 6(17):4233–4239, 2004.

[22] Hindmarsh, William Russell and Judith M Farr. "Collision broadening of spectral lines by neutral atoms". *Progress in Quantum Electronics*, 2:141–214, 1973.

[23] Izotova, SL, AI Kantserov, and MS Frish. "Constants for broadening and shift of D_1 and D_2 rubidium-87 lines by inert gases". *Optics and Spectroscopy*, 51:107–109, 1981.

[24] Kantor, P Ya and LN Shabanova. "Profiles of the Rbi 794.7-and 780.0-nm lines in the presence of inert gases; parameters of interatomic potentials". *Optics and Spectroscopy*, 58:614–619, 1985.

[25] Kazantsev, SA, NI Kaliteevskii, and OM Rish. "Application of the magnetic scanning technique for measuring the broadenings and shifts of the D_1 resonance line of rubidium caused by inert gases". *Optics and Spectroscopy*, 44:372–375, 1978.

[26] Kielkopf, John F. "Predicted alkali collision broadening by noble gases based on semiempirical potentials". *Journal of Physics B: Atomic and Molecular Physics*, 9(17):L547, 1976.

[27] Kluttz, Kelly A., Todd D. Averett, and Brian A. Wolin. "Pressure broadening and frequency shift of the D_1 and D_2 lines of Rb and K in the presence of ^{3}He and N_2". *Physical Review A*, 87:032516, 2013.

[28] Krupke, William F. "Diode-pumped alkali laser", 2003. US Patent 6,643,311.

[29] Krupke, William F. "Diode pumped alkali lasers (DPALs) - A review (rev1)". *Progress in Quantum Electronics*, 36(1):4–28, 2012.

[30] Krupke, William F, Raymond J Beach, V Keith Kanz, and Stephen A Payne. "Resonance transition 795-nm rubidium laser". *Optics Letters*, 28(23):2336–2338, 2003.

[31] Langhoff, PW and M Karplus. "Pade summation of the cauchy dispersion equation". *Journal of the Optical Society of America*, 59(7):863–871, 1969.

[32] Larson, B, O Hausser, PPJ Delheij, DM Whittal, and D Thiessen. "Optical pumping of Rb in the presence of high-pressure He 3 buffer gas". *Physical Review A*, 44(5):3108, 1991.

[33] Loper, Robert D. *Collisional broadening and shift of D1 and D2 spectral lines in atomic alkali vapor-noble gas systems*. PhD Dissertation, Air Force Institute of Technology, 2013.

[34] Mastromarino, PA, CR Otey, D Pripstein, and EW Hughes. "Tunable diode laser study of pressure broadening of Rb D_1 lines in the presence of ^{4}He buffer gas". *Nuclear Instruments and Methods in Physics Research Section B: Beam Interactions with Materials and Atoms*, 194(1):69–77, 2002.

[35] Merritt, Jeremy M, Jiande Han, Terry Chang, and Michael C Heaven. "Theoretical investigations of alkali metal: rare gas interaction potentials". *SPIE LASE: Lasers and Applications in Science and Engineering*, 71960H–71960H. International Society for Optics and Photonics, 2009.

[36] Miller, WS, CV Sulham, JC Holtgrave, and GP Perram. "Limitations of an optically pumped rubidium laser imposed by atom recycle rate". *Applied Physics B*, 103(4):819–824, 2011.

[37] Moore, CE. "Atomic energy levels NSRDS-NBS". *Circular No. 467*, volume 2. US GPO Washington, 1971.

[38] Müller, Wolfgang, Joachim Flesch, and Wilfried Meyer. "Treatment of intershell correlation effects in abinitio calculations by use of core polarization potentials. Method and application to alkali and alkaline earth atoms". *The Journal of Chemical Physics*, 80(7):3297–3310, 1984.

[39] Nesmeyanov, Andrei Nikolaevich and JI Carasso. *Vapour pressure of the elements*. Infosearch, 1963.

[40] Ottinger, Ch, Richard Scheps, GW York, and Alan Gallagher. "Broadening of the Rb resonance lines by the noble gases". *Physical Review A*, 11(6):1815, 1975.

[41] Pitz, Greg A, Charles D Fox, and Glen P Perram. "Pressure broadening and shift of the cesium D_2 transition by the noble gases and N_2, H_2, HD, D_2, CH_4, C_2H_6, CF_4, and He_3 with comparison to the D_1 transition". *Physical Review A*, 82(4):042502, 2010.

[42] Pitz, Greg A, Gordon D Hager, Tiffany B Tafoya, Joseph W Young, Glen P Perram, and David A Hostutler. "An experimental high pressure line shape study of the rubidium D_1 and D_2 transitions with the noble gases, methane, and ethane". *SPIE LASE*, 896208–896208. International Society for Optics and Photonics, 2014.

[43] Pitz, Greg A, Douglas E Wertepny, and Glen P Perram. "Pressure broadening and shift of the cesium D_1 transition by the noble gases and N_2, H_2, HD, D_2, CH_4, C_2H_6, CF_4, and He_3". *Physical Review A*, 80(6):062718, 2009.

[44] Romalis, MV, E Miron, and GD Cates. "Pressure broadening of Rb D_1 and D_2 lines by ^{3}He, ^{4}He, N_2, and Xe: Line cores and near wings". *Physical Review A*, 56(6):4569, 1997.

[45] Rotondaro, Matthew D and Glen P Perram. "Collisional broadening and shift of the rubidium D_1 and D_2 lines ($5^2S_{1/2} \rightarrow 5^2P_{1/2}$, $5^2P_{3/2}$ by rare gases, H_2, D_2, N_2, CH_4 and CF_4". *Journal of Quantitative Spectroscopy and Radiative Transfer*, 57(4):497–507, 1997.

[46] Roueff, E and A Suzor. "Broadening, shift and depolarization of broad fine structure alkali spectral lines by helium". *Journal de Physique*, 35(10):727–740, 1974.

[47] Shang-Yi, Ch'en. "Broadening, asymmetry and shift of rubidium resonance lines under different pressures of helium and argon up to 100 atmospheres". *Physical Review*, 58:1051–1058, 1940.

[48] Tang, KT and J Peter Toennies. "An improved simple model for the van der Waals potential based on universal damping functions for the dispersion coefficients". *The Journal of Chemical Physics*, 80(8):3726–3741, 1984.

[49] Tsi-Zé, Ny et al. "Pressure Effects of Rare Gases on the Second Doublet of Rubidium Principal Series". *Physical Review*, 52(11):1158, 1937.

[50] Wilson, John Norton and Richard M Curtis. "Dipole polarizabilities of ions in alkali halide crystals". *The Journal of Physical Chemistry*, 74(1):187–196, 1970.

[51] Zameroski, Nathan D, Gordon D Hager, Wolfgang Rudolph, Christopher J Erickson, and David A Hostutler. "Pressure broadening and collisional shift of the Rb D_2 absorption line by CH_4, C_2H_6, C_3H_8, n-C_4H_{10}, and He". *Journal of Quantitative Spectroscopy and Radiative Transfer*, 112(1):59–67, 2011.

[52] Zweiback, J, A Komashko, and WF Krupke. "Alkali-vapor lasers". 75810G–75810G, 2012.